

Printed Silver Electrode for Silicon-based Schottky Barrier Diode: High Rectification Ratio Enabled by Ag/*p*-Si Interface Exceeds Theoretical Barrier Height

Masashi Saitoh^{1,*} and Toshiyuki Tamai^{1,†}

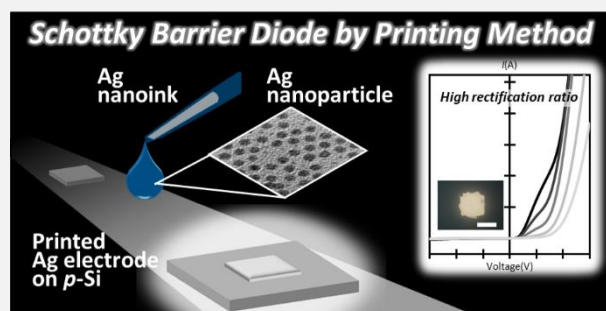
Affiliations:

¹Osaka Research Institute of Industrial Science and Technology (ORIST), Osaka, 536-0025, Japan.

Contact Address:

*smasashi@omtri.or.jp, †tositama@omtri.or.jp

Abstract: The printed electronics enables the fabrication of a variety of devices and is becoming important as critical techniques for some applications in diverse areas. Fine line fabrication, variation of materials, and improvement of processes have been demonstrated, however the junctions formed at the contact between printed electrodes and semiconductors remain a crucial challenge. In this paper, we performed the first demonstration of the silicon-based Schottky barrier diode (SBD) by printing method, where the silver (Ag) electrode was



fabricated through the printing of the Ag nanoink on p-type silicon (*p*-Si) and sintering at 300 °C. Measurement of I-V characteristics, scanning electron microscopy (SEM) and atomic force microscopy (AFM) together with Kelvin probe force microscopy (KPFM) were performed for understanding the interface between Ag and *p*-Si (Ag/*p*-Si interface). The analyses of I-V data showed the fabricated SBDs by printing method have typical Schottky contact behavior with relatively high rectification ratio, where Schottky parameters were successfully estimated and showed sintering time dependent behavior. Of some Schottky parameters, ideal factors and parallel series resistances increased with sintering time and these increments are found to be responsible for the vacancy in the Ag electrodes at the Ag/*p*-Si interface from SEM observations. From AFM/KPFM measurements, we discussed the possible mechanism of the increment of Schottky barrier height in the SBDs, in which the depth of the depletion layer can be modulated by the existence of Ag nanoparticles at the Ag/*p*-Si interface. In conclusion, the performance of the SBDs is found to be responsible for the unexpected morphological effect at the Ag/*p*-Si interface exceeds theoretical barrier height.

Introduction

Understanding and engineering of the junctions formed at the contact interface between metallic electrodes and semiconductor materials are key elements in modern electronic devices. With much research effort and development of technologies, various methods have been established to make the ideal interface between metal (M) and semiconductor (S) (M/S interface) achieve theoretically predicted performances.^{1,2} One of the most important parameters for M/S interface is the Schottky barrier height (SBH) because the SBH fundamentally determine the current conduction across the M/S interface and then impact of the device performances. In the ideal M/S interface, the SBH value can be theoretically predicted based on the Schottky-Mott rule, where the value can be expressed by the work function of metal and the Fermi level of semiconductor.³ Because of the simplicity of designing M/S interface, some attempts at the M/S interface leads to some interesting results in

the tunability of SBH, achieving desirable electrical properties in the devices.⁴ Especially for Schottky barrier diode (SBD), the SBH value has a direct effect on characteristic parameters of the SBD, for example, working voltage, rectification ratio and switching rate, respectively. However, the high-energy methods such as sputtering, vacuum deposition, plating, and photolithography is mainly used for creating the ideal M/S interface, in which multi-staged masking and etching under highly vacuumed environment and use of harmful and environmentally undesirable chemical are required. On the other hand, as one of the low-energy methods, noble approach of van der Waals junctions are developed very recently, in which metal electrodes with atomically flat surfaces are fabricated and laminated onto semiconductors.^{5,6} In the approach, however, the applicable metals and semiconductors are currently limited to some candidates. Moreover, the performances of the devices are also limited, because I-V relationship is to be

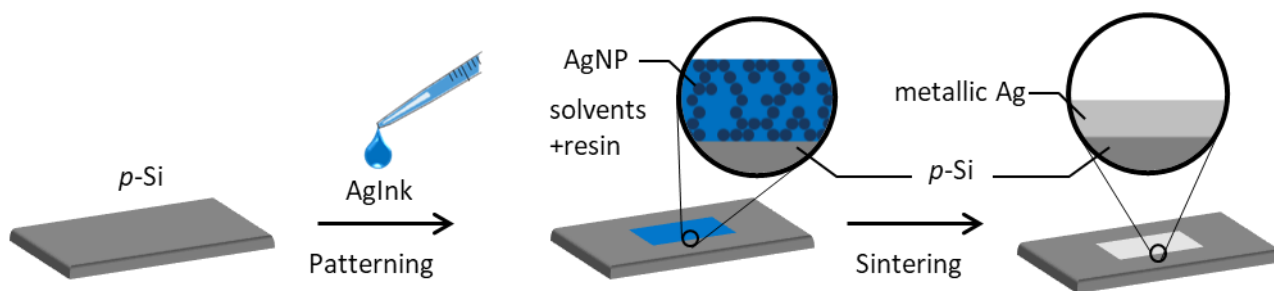


Figure 1. Representative illustration of the fabrication of SBD by printing method. Patterning of AgInk was conducted on p -Si, in which the AgInk was composed of the AgNPs, solvents and a resin. After sintering, together with transformation of patterned AgInk to metallic Ag electrode, Ag/ p -Si interface was formed.

determined by work function of metal and Fermi level of semiconductor according with the Schottky-Mott rule. During the course of securing alternatives for ecofriendly and widely applicable methods, the printed electronics (PE) has been emerged as one of alternative methods for making the practical devices using conductive inks.⁷⁻¹¹ Though PE is one of the printing technologies specified into electronic manufacturing with the usage of the traditional printing methods, PE is an advantageous and promising method as not only ecofriendly but also cost-effective process compared with traditional processes. In addition, PE is a promising technology for enabling flexible and wearable smart devices to be compatible with various plastic materials and papers, achieving the fabrication of electronic devices with some advantages of slight-weight, flexible, and foldable which are highly demanded in the next-generation smart electronics.¹²⁻¹⁴ Since, to date, fine-line fabrication,^{15,16} variation of materials,^{10,17,18} and improvement of processes¹⁹⁻²¹ have been demonstrated in the development of PE, PE enables the fabrication of a variety of devices and is becoming important as critical techniques for some applications in diverse areas.

However, despite much effort over the decades in the PE field, the junctions formed at the contact between a printed electrode and a semiconductor remains a crucial challenge. Moon *et al.* provided the careful description of the silver (Ag)/organic semiconductor interface created by ink-jet method with Ag nanoparticle ink.²² They observed that ligand molecules capped on Ag nanoparticles induce an interface dipole, which causes an increase in the work function of the resulting printed electrodes. This work showed the work function of the metal electrodes made from metal nanoparticle ink could be modulated by the electronic disturbance induced when metal nanoparticle transformed into Ag electrode. Though the understanding and engineering of junctions formed at the M/S interface with the printing method open new way to modulate the SBH and then device performances, methodologies using the printing method have not been sufficiently explored. In addition, there are few researches on

silicon (Si) substrates with metal electrode made by the printing method even though Si is one of the widely used semiconductors in practical. Because of deviation between theory and experiments in Si-based electrical devices which is mainly originated from surface oxidation, systematic investigations have not conducted for the electrical properties and morphological observations in the interface between metal electrode and Si substrate. Fine tuning of SBH between metal electrode and Si can provide benefits of achieving high-speed operations and low-voltage drives of thin field transistors, and/or high efficient energy conversions of solar cells.

In this study, for the first time, fabrication of the SBD on p -type Si (p -Si) by printing method was achieved using Ag nanoink (AgInk) as shown in Figure 1. Firstly, the synthesis of Ag nanoparticles (AgNPs) were successfully demonstrated, in which AgNPs were designed in order to be dispersed in organic solvents, and transformed into metallic film when sintering. Next, AgInk was made from the lab-made AgNPs, solvents and a resin, in which the composition of AgInk was adjusted for patterning by squeegee method. After sintering at 300 °C, the obtained metallic Ag film showed low sheet resistance enough to work as electrode.

When the Ag electrode was patterned onto p -Si using AgInk, the obtained device was found to show typical SBD characteristics from I-V measurements. When analyzing I-V characteristics of the SBDs using Schottky diode model, the unprecedented high SBH values were found compared with a reference of a vacuum-deposited Ag electrode. To elucidate the mechanism of high SBH, scanning electron microscopy and scanning probe microscopy were employed to investigate the morphological structures and surface potential at the interface between printed Ag and p -Si (Ag/ p -Si interface).

Results and Discussion

Preparation of AgNPs and AgInk

AgNPs were synthesized based on a previously reported method^{23,24} with slight modification, in which Ag precursor complex reacted with reducing reagents and capping molecules

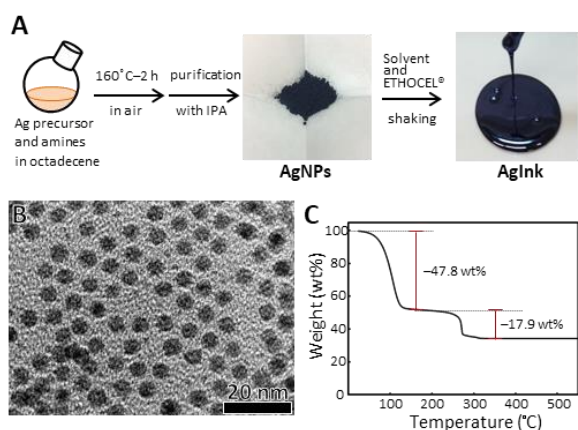


Figure 2. Preparation of AgNPs and AgInk. (A) Representative process for preparing AgNPs followed by AgInk. (B) TEM image of AgNPs. (C) TG profile of AgInk.

at the temperature of which the complex decomposes. In this study, as a precursor complex, Ag(I) octanoate was used for synthesizing AgNPs with a uniform diameter, resulting the transformation of AgNPs to metallic Ag can occur at the narrow range of sintering temperature. As shown in Figure 2A, Ag(I) octanoate was mixed with octadecylamine as reducing reagent and tetradecanoic acid as capping molecules in 1-octadecene and reacted at 180 °C for 2h. After purification by decantation with isopropanol followed by dry at ambient temperature, AgNPs were obtained with a multi-gram scale as shown in Figure 2A. The AgNPs were could be dispersed in various non-polar organic solvents such as hexane and toluene. Figure 2B shows a transmission electron microscopy (TEM) image of AgNPs. From TEM observations, the diameter of the AgNPs were found to be almost uniform (average diameter is 8.7 nm, size deviation is 8.6 % as counts of 100 NPs).

Next, AgNPs were mixed with a solution composed of *p*-tert butyltoluene, 2-phenylethan-1-ol and ETHOCEL® using with a planetary mixing apparatus. After mixing, the AgNPs were dispersed uniformly and then AgInk was obtained as a slightly viscous solution (Figure 2A). Figure 2C shows a thermogravimetric (TG) profile of AgInk, in which a heating rate set at 20 °C·min⁻¹ under an air flow of 300 mL·min⁻¹. In the TG profile, weight decreases in two steps. The first decrease in weight around 86 °C (-47.8 wt%) corresponds to vaporization of solvents, and the second decrease around 247 °C (-17.9 wt%) to the thermal decomposition of the ETHOCEL® and capping molecules. From TG analysis, Ag content of AgInk was determined to be 34.3 wt%. Moreover, differential thermal analysis (DTA) measured along with TG showed exothermic peaks in DTA spectra in the temperature range of around 262-276 °C, indicating the coalescence of AgNPs, which means transformation of AgNPs into metallic Ag occurs in this temperature range.

Formation of Ag electrode on *p*-Si and electrical characteristics

From TG analysis of AgInk, the sintering temperature of 300 °C is selected since it is enough to make Ag electrode work while thermal damage to Ag/*p*-Si interface should be minimized during the sintering procedure. To investigate the electrical characteristics by sintering, AgInk was patterned onto glass and sintered at 300 °C for 5–30 min. As shown in Figure 3A, patterned AgInk transformed into metallic-colored Ag thin films in each sintering times. The results of sheet resistance of the films as a function of the sintering time are shown in Figure 3B. As increasing sintering time, sheet resistance decreases from

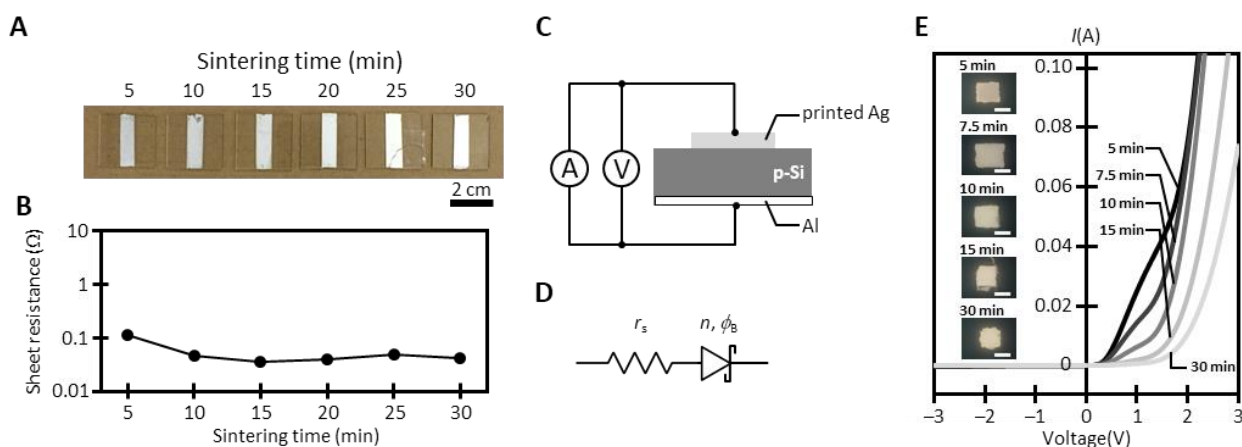


Figure 3. Formation of Ag electrode and electrical characteristics on *p*-Si (sintering temperature is 300 °C). (A) Photo images of Ag thin films on glass with sintering time of 5–30 min. (B) Sheet resistance of the Ag thin films as a function of sintering time. (C) An experimental set-up for I-V measurement of the printed SBD. (D) An equivalent circuit of the SBD: n is ideal factor, ϕ_B is SBH, and r_s is series resistance. (E) I-V characteristics of the SBDs with the sintering time of 5 min, 7.5min, 10 min, 15 min, and 30 min. In insets, microscopic photographs of Ag electrodes are shown (all scale bars in the insets are 1 mm).

0.114 Ω/\square at 5 min to 0.046 Ω/\square at 10 min and becomes constant to be c.a. 0.04 Ω/\square from 10 min to 30 min. These results mean sintering process of AgInk ends up to 15 min completely, where the solvent and the resin in the AgInk are evaporated and decomposed, followed by adhering AgNPs through decomposition of capping molecules on surfaces and grain boundary diffusion. Using the value of film thickness measured from scanning electron microscopic (SEM) observations (vide infra), the electrical resistivity of Ag film is estimated to be $2 \times 10^{-5} \Omega \cdot \text{cm}$ at 15 min which is only an order of magnitude higher than the resistivity of metal Ag ($1.6 \times 10^{-6} \Omega \cdot \text{cm}$). Generally, the electrical resistivity of the electrodes made from conductive inks tends to be larger, where the increment can be resulted from some reasons such as organic residuals and boundary defects, so on.²⁵

Since a low resistivity was achieved using with AgInk, Ag electrode was also formed on *p*-Si by squeegee method as one of printing methods. The resulting SBD showed typical diode characteristics, which is the first demonstration of the silicon-based SBD fabricated by printing method (printed SBD). Figure 3C and D show an experimental set-up for I-V measurement of the printed SBD and the equivalent circuit of the printed SBD, respectively. As the SBD structure, square shaped Ag electrodes (designed size is $0.15 \times 0.15 \text{ cm}^2$) were formed on a side of the *p*-Si. On the other side of the *p*-Si, an aluminium (Al) ohmic contact was provided by vapor deposition (Figure 3C). In the structure, Ag/*p*-Si interface should show the electrical behavior of the SBD, which are predicted from the work function of Ag²⁶ and the Fermi-level of Si. And the SBH for the ideal diode of evaporated Ag electrode formed on *p*-Si have been reported to be 0.55–0.54 eV.^{27,28} Such a SBD can be represented by the equivalent circuit of Figure 3D, consisting of ideal factor (*n*), SBH (ϕ_B), and series resistance (r_s). Figure 3E shows a set of I-V measurements and microscopic photographs for the printed SBDs with different sintering time (5, 7.5, 10, 15, 30 min).

From microscopic photographs in the inset of Figure 3E, Ag electrodes were successfully formed onto the *p*-Si and their effective areas are listed in Table 1. In the I-V measurements, forward and reverse I-V characteristics showed a behavior of typical diode and the device performance of the printed SBDs depends on the sintering time. The on/off current ratios (rectification ratios) in the printed SBDs were higher than that of the vacuum-deposited SBD and these ratios increased with sintering time, indicating an improvement of on/off performance of the SBD. These rectification ratios are summarized in Table 1. Furthermore, the shoulder appeared around the voltage of 1 V in the printed SBD of 5min and then it gradually decreased with the sintering time. The shoulder represents an excess current component which can be induced

by inhomogeneous contact at the Ag/*p*-Si interface. On the other hand, the Ag electrode prepared by vacuum deposition showed a relatively low electrical resistivity ($2.1 \times 10^{-6} \Omega \cdot \text{cm}$) which is an almost equivalent to that of metal Ag ($1.6 \times 10^{-6} \Omega \cdot \text{cm}$). The vacuum-deposited SBD, however, exhibits low rectification ratio (2.04×10^2) in spite of its highest conductivity of the electrode. This implies that the conductivity of the electrode itself is irrelevant to the device performance. Thus, the high rectification ratio of the printed SBD and their I-V characteristics depended on the sintering time cannot be explained in terms of the physical properties of the electrode, such as the conductivity.

I-V analysis of the printed SBD as a function of the sintering time

Forward I-V characteristics of a series of printed SBDs represented in Figure 3E were used to extract Schottky parameters in order to investigate the effect of the sintering time. Among some methods proposed to deduce the Schottky parameters from forward I-V characteristics,^{29–33} we used the method by Cheung *et al.*³⁴ because of high applicable for our results. The forward I-V characteristics of the diode obeying the thermionic emission model are given by equation (1),

$$I = A_{\text{eff}} A^* T^2 \exp(-\beta \phi_B) \left[\exp \left\{ \frac{\beta}{n} (V - I r_s) \right\} - 1 \right] \quad (1)$$

$$\beta = \frac{q}{kT}$$

where A_{eff} , A^* , T , $q\phi_B$, n , and r_s are effective area of the diode, Richardson constant, absolute temperature, Schottky barrier height, ideality factor, and series resistance, respectively. The constant value of β is $38.9 \text{ C} \cdot \text{J}^{-1}$ at the room temperature ($T = 298 \text{ K}$) where q and k are electronic charge and Boltzmann constant, respectively. The Richardson constant, A^* is $32 \text{ A} \cdot \text{cm}^{-2} \cdot \text{K}^{-2}$ for *p*-Si.³⁵ The ideality factor, n is included to take into account non ideal diode behaviors, where n is equal to 1 for the ideal diode. Generally, n becomes more than 1 for the real device because n varies mainly depending on physical processes for carrier transport across the M/S interface of the diode. The equation (1) is derived to equation (2) in the case of $V - I r_s > 3kT/q$ ($\sim 0.08 \text{ V}$ at 298 K).

$$J = A^* T^2 \exp(-\beta \phi_B) \exp \left\{ \frac{\beta}{n} (V - I r_s) \right\} \quad (2)$$

Equation (2) can be rewritten in terms of current density, J ($=I/A_{\text{eff}}$).

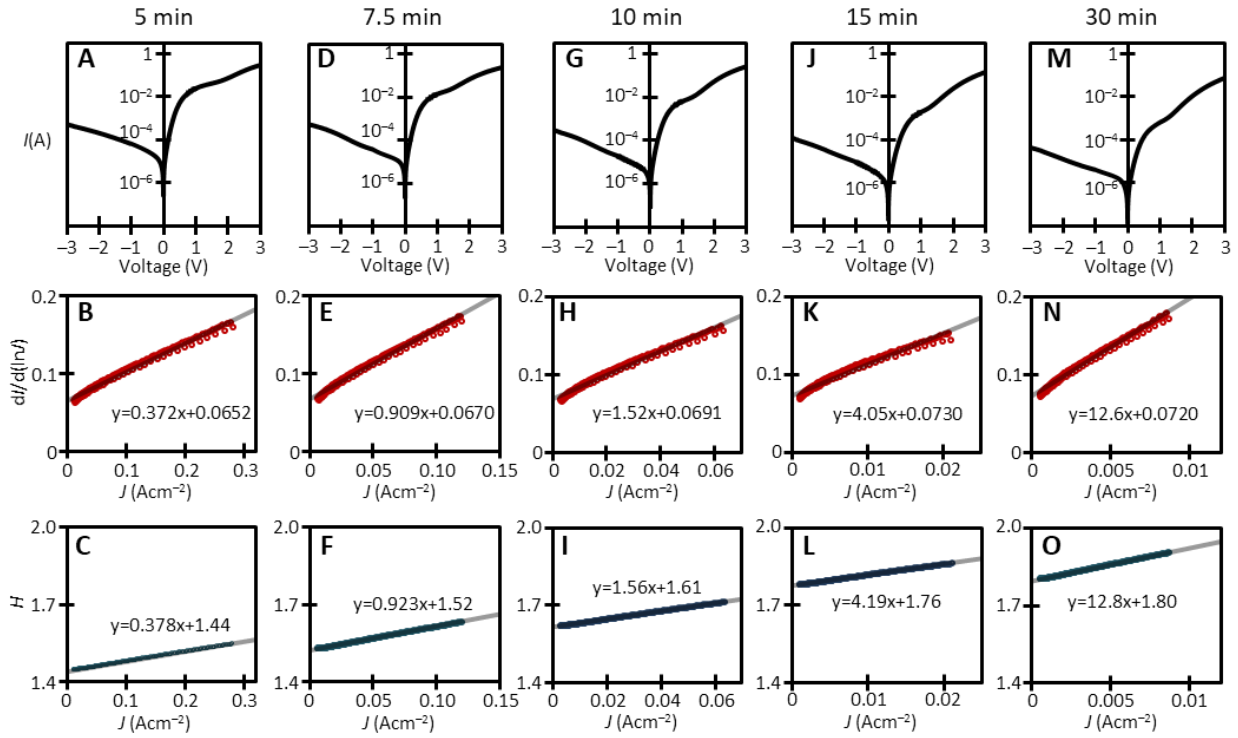


Figure 4. I-V analysis of the printed SBDs for the sintering time of (A–C) 5 min, (D–F) 7.5 min, (G–I) 10 min, (J–L) 15 min, and (M–O) 30 min. (A, D, G, J, M) Logarithmic form of I-V. (B, E, H, K, N) Plots of $dV/d(\ln J)$ as a function of J as open circles. (C, F, I, L, O) Plots of H as a function of J as open circles. Lines from the least square method and the corresponding formula are shown in each Figures.

$$V = Ir_s + \frac{n}{\beta} \ln \frac{J}{A \cdot T^2} + n\phi_B \quad (3)$$

Differentiating equation (3) with respect to $\ln J$, equation (4) is obtained. Moreover, a function $H(J)$ can be defined as equation (5).

$$\frac{dV}{d(\ln J)} = A_{eff} r_s \cdot J + \frac{n}{\beta} \quad (4)$$

$$H = V - \frac{n}{\beta} \ln \frac{J}{A \cdot T^2} = A_{eff} r_s \cdot J + n\phi_B \quad (5)$$

Using equation (4), a plot of $dV/d(\ln J)$ vs. J will give a straight line with the slope of $A_{eff} \cdot r_s$ and the intercept of n/β , determining the n value. On the other hand, using equation (5), a plot of $H(J)$ vs. J will give a straight line with the intercept of $n\phi_B$, and then ϕ_B is determined from the n value. Equation (4) and (5) were applied to extract the Schottky parameters of a series of printed SBDs and a vacuum-deposited SBD, respectively. For the I-V data in the range of 0.2–0.5 V, plots of $dV/d(\ln J)$ and $H(J)$ are shown in Figure 4 B, E, H, K, N and

C, F, I, L, O, respectively. Each experimental plots are on a straight line, indicating the good agreement with the diode equation. Thus, these results confirm the validity of equation (4) and (5) in the selected voltage range. By fitting the plots by the least square method, the Schottky parameters of a series of printed SBDs and a vacuum-deposited SBD were determined and summarized in Table 1.

From Table 1, Schottky parameters (n , r_s , and $q\phi_B$) increased with the sintering time. For the printed SBDs, n is larger than 2.5, which is much larger than the value for the vacuum-deposited SBD ($n = 1.16$). In general, the relatively high n implies the formation of an oxide layer at the M/S interface. The relatively high value of r_s also implies the existence of an oxide layer at the interface. However, cross-sectional SEM observations with elemental analysis of the Ag/p-Si interface indicate no evidence of the existence of an oxide layer in the experimental resolution (Figure 5, vide infra). Non-existence of an oxide layer strongly suggests that the removal of the native oxide layer and the joining Ag and p-Si took place in order at the first stage of the sintering process. In the sintering process, removing of capping reagents covering AgNPs occurred around 247 °C (vide supra) followed by the decomposition of the reagents through an oxidation reaction at the same temperature. Thus, this oxidation reaction can

Table 1. Effective area and extracted diode parameters for the printed and vacuum-deposited SBDs in the I-V analysis.

SBD	Sintering time (min)	A_{eff} (cm ²) ^a	Rectification ratio ^b	n^c	r_s (Ω) ^c	$q\phi_b$ (eV) ^c
Printed	5	0.0183	5.83×10^2	2.54	20.4	0.569
	7.5	0.0275	4.16×10^2	2.61	33.0	0.584
	10	0.0206	8.49×10^2	2.69	73.8	0.601
	15	0.0153	1.03×10^3	2.84	265	0.625
	30	0.0156	1.60×10^3	2.80	827	0.641
Vacuum-deposited	—	0.0100	2.04×10^2	1.16	13.6	0.500

^a Measured from microscopic photographs shown in Figure 3E. ^b Recorded at ± 3.0 V. ^c Estimated from the I-V data in the range of 0.2–0.5 V.

involve the removal of the oxide layer on the *p*-Si surface, and then the bared AgNPs can be attached and joined to the *p*-Si surface, creating an interface that is free from the oxide layer.^{36,37} Also, in particular, the surface energy effect of the AgNPs should facilitate this joining process. Consequently, joining between Ag and *p*-Si achieved in sintering process causes the high interfacial strength. Therefore, the increment of n and r_s with the sintering time cannot be attributed to the oxide layer. Moreover, the possible explanation should interpret the relatively high $q\phi_b$ with the increase of sintering time. From the work function of Ag and the Fermi-level of lightly-doped *p*-Si, theoretical SBH is predicted to be 0.52 eV for Ag/*p*-Si, and good agreement with experimental data have been reported.^{27,28} However, in our results, though $q\phi_b$ of a vacuum-deposited SBD (0.500 eV) shows good agreement with reported data, a

series of $q\phi_b$ of printed SBDs are high of 0.069–0.141 eV compared with a vacuum-deposited SBD and showed tendency to increase with sintering time.

Morphological observation of the printed Ag electrode and Ag/*p*-Si interface

To investigate the effect of the roughness at the Ag/*p*-Si interface to increment of n , r_s and $q\phi_b$, surface and cross-sectional SEM observations were performed for the printed SBDs of sintering time of 5, 7.5, 10, 15, 30 min. It is reported that the local work function of vacuum-deposited Au layers on Cu are lower of c.a. 0.8 eV at the step edges,³⁸ which strongly indicates the $q\phi_b$ can be modified by the roughness at the Ag/*p*-Si interface. Figure 5A, D, G, J, M represent surface observations of the printed Ag electrodes. At the sintering time of 5 min (Figure 5A), AgNPs

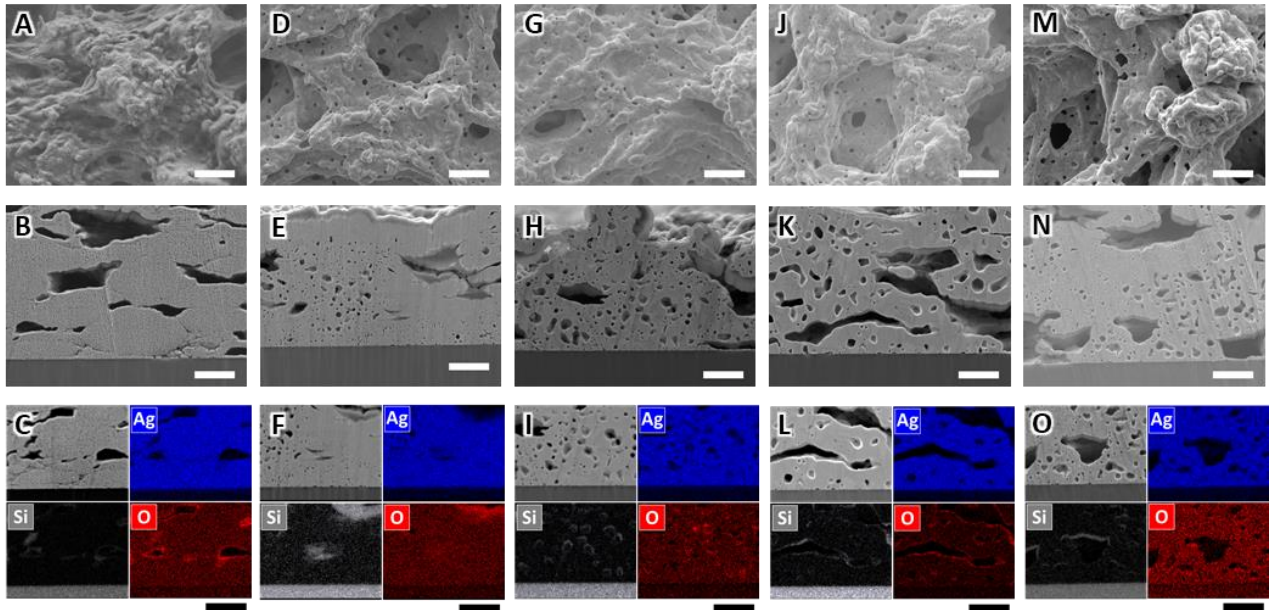


Figure 5. SEM observations of a series of printed SBDs for the sintering time of (A–C) 5 min, (D–F) 7.5 min, (G–I) 10 min, (J–L) 15 min, and (M–O) 30 min. (A, D, G, J, M) Surface observations of the printed Ag electrodes. (B, E, H, K, N) Cross-sectional observations at the Ag/*p*-Si interface. (C, F, I, L, O) EDX elemental mappings (Ag, Si and O) at the Ag/*p*-Si interface. All scale bars are 2 μ m.

started to melt and coalesce, forming continuously interconnected networks. Over the surface, 2–5 μm size of pores were observed, which can be formed by removal of the solvents and the resin during drying and/or the first stage of the sintering. At the sintering time of 10 min (Figure 5D), AgNPs merged further, appearing 100–200 nm size of pores, which can be attributed to combustion of capping reagents on AgNPs. Subsequently there is no significant change in the morphology of the surface (Figure 5G, J, M).

Similar morphological results were obtained in the cross-sectional observations as shown in Figure 5B, E, H, K, N. These morphological results are qualitatively agreement with the increment of n and r_s because, due to the formation of pores near the Ag/ p -Si interface, the contact at the interface deviates from the ideal contact and also the fluency of electrons and holes is hindered. On the other hand, from the cross-sectional observations, Ag electrodes connected to p -Si and form smooth Ag/ p -Si interface. There is no evidence indicating the existence of the step edges which can induce the increment of the local work function. Moreover, from the EDX elemental mapping of the cross-sections as shown in Figure 5C, F, I, L, O, there is no evidence of an oxide layer and/or an alloyed layer at the Ag/ p -Si interface. Thus, the increment of $q\phi_B$ of the printed SBDs and their dependence on the sintering time cannot be explained in terms of the morphological effects of the electrode at the Ag/ p -Si interface.

AFM and KPFM mapping by scanning probe microscopy (AFM/KPFM)

For investigation of the increment of $q\phi_B$ in a series of printed SBDs, in this section, we have quantified the magnitude of the surface topography and the surface potential at the Ag/ p -Si interface by performing atomic force microscopy (AFM) measurements together with Kelvin probe force microscopy (KPFM).^{39–42} The experimental setup is shown in Figure 6A, where a sample is placed on the piezo-stage and scanned by a conductive AFM probe (PtSi) attached on the tip of the cantilever. The probe approaches to a sample and then scans along the sample surface while keeping the oscillating force on the probe constant, resulting in a topographic image of the surface. Additionally, using KPFM, the surface potential image and the topographic data can be obtained simultaneously at every measuring point. When the probe is held close to the sample surface, the force acting on the probe consists of the electrostatic force caused by the contact potential difference (CPD) between the probe and the sample as shown in Figure 6A. To observe the topographic and potential images at the Ag/ p -Si interface, the preparation of experimental samples is well designed as shown in Figure 6B. All experiments were conducted under ambient condition.

Figure 6C–G shows the topographical images of the printed Ag electrodes at the Ag/ p -Si interface. At the sintering time of 5 min (Figure 6C), the surface was observed to be wavy, this indicates that the removal of solvents and organics in AgInk followed by the aggregation of AgNPs formed 1–2 μm size of aggregates. At the sintering time of 10 min (Figure 6D), 100–200 nm size of pores were observed, which can be attributed to heat shrinkage of the aggregated AgNPs. Subsequently, as the melting and aggregating of AgNPs proceed throughout the overall sample, the surface becomes to be smooth. The morphological change of the surface is observed to be diminished in the sintering time of 15 min (Figure 6E–G). The surface averaged roughness of each images is calculated and summarized in Table 2. The numerical aspect also indicates that the surface of the Ag electrodes at the Ag/ p -Si interface becomes smooth with the sintering time. These morphological change with the sintering time are good accordance with the results of SEM observations (vide supra). Though the surface were observed to be almost flat from the topographic image in the sintering time of 30 min, the surface roughness value (3.8 nm) did not decrease to the value of the vacuum-deposited electrode (2.8 nm), which implies that some AgNPs exist in the surface and are involved in electrical contact at the interface.

Figure 6H–L shows CPD images of the Ag electrodes at the Ag/ p -Si interface. In the sintering time of 5 min (Figure 6H) and 10 min (Figure 6I), the distribution of CPD in the images was observed to be inhomogeneous. And then, the distribution of CPD gradually became homogeneous with the sintering time. At the sintering time of 30 min, the CPD is the almost same at every measured points. Furthermore, there is no correlation between the CPD value and the surface roughness as shown from height and CPD profiles along the same line in each images. The surface-averaged CPD of each image is calculated and summarized in Table 2, where the surface-averaged CPD is found to decrease with sintering time. The decrease of CPD strongly implies that the electrical potential of the Ag electrodes at the interface intrinsically decreases.

For comparison of the $q\phi_B$ estimated from the I-V data of the printed SBDs, the work function of the printed Ag electrodes are estimated from the surface-averaged CPD by referring to the work function of Au (5.10 eV)²⁶ and listed in Table 2. The estimated work function of vacuum-deposited Ag electrode is 4.68 eV which is very close to the value of Ag (100) (4.64 eV),^{26,42} indicating that our estimation is reasonable for the printed Ag electrodes. In the sintering time of 5 min, the work function is 4.49 eV which is lower than the value of vacuum-deposited Ag electrode (4.68 eV), indicating the residual of organics from ligand molecule capping on AgNPs and/or the

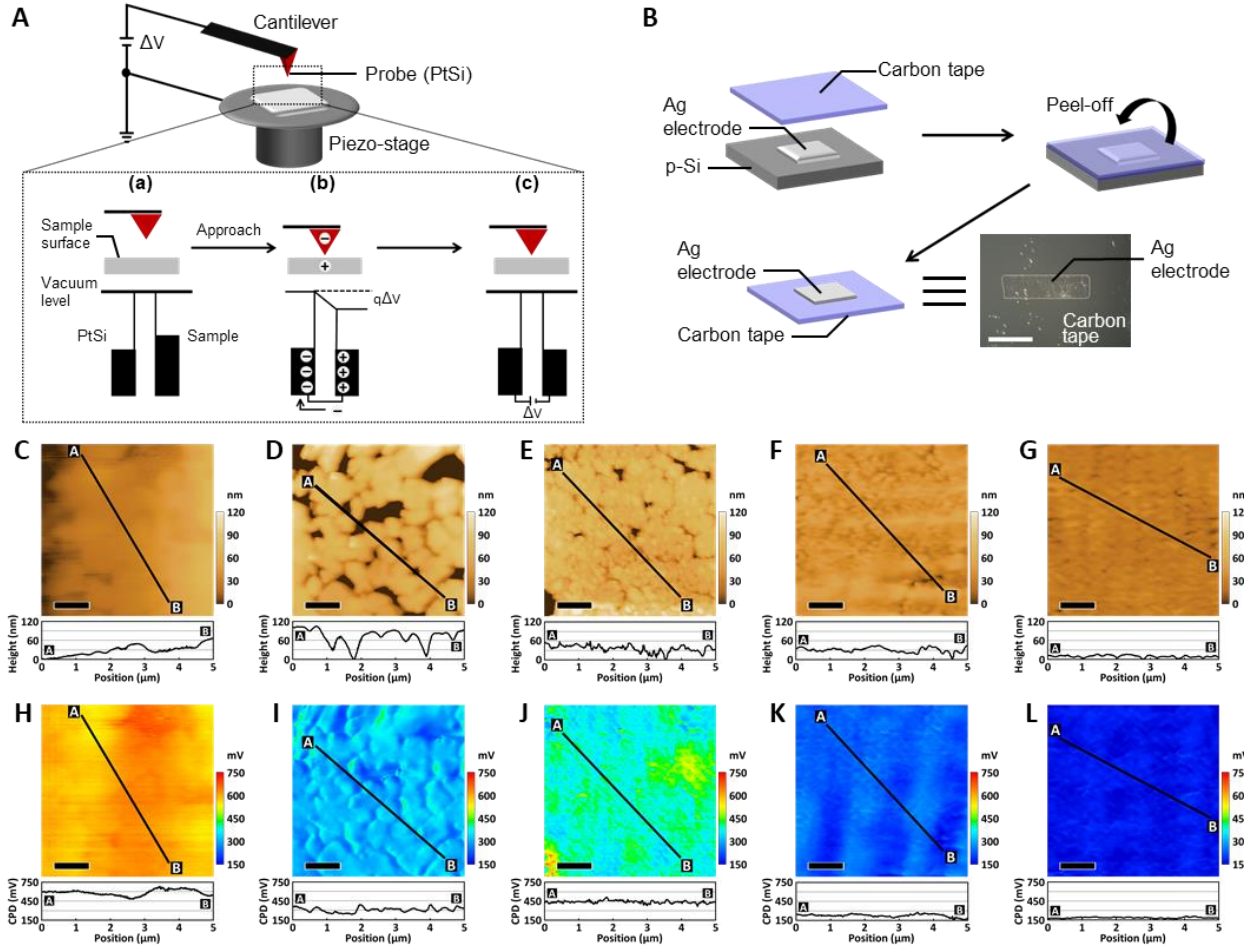


Figure 6. AFM/KPFM of the printed Ag electrodes. (A) A schematic illustration of AFM-based KPFM for measuring surface potential. Electronic energy levels of the probe and the sample for KPFM: (a) probe approaches to the sample surface, (b) probe and sample are in electrical contact and the electrostatic force caused by the CPD ($q\Delta V$), and then (c) external bias (ΔV) is applied to nullify the CPD, and thus the electrostatic force. (B) Schematic illustration of sample preparation for AFM/KPFM measurements. A dotted line is the guideline indicating the Ag electrode transferred on the carbon tape. A scale bar in the inset picture is 1 mm. (C–G) AFM and (H–L) KPFM images of the printed Ag electrodes for the sintering time of (C, H) 5 min., (D, I) 7.5 min., (E, J) 10 min., (F, K) 15 min., and (G, L) 30 min. All scale bars are 1 μm . Height and CPD line profiles are indicated by lines in each images.

resin as an additive in AgInk. In further sintering, the work functions of the printed Ag electrodes increased and they all were high compared with that of vacuum-deposited Ag electrode (4.68 eV). However, these results are not accordance with the increment of $q\phi_B$ in the printed SBDs, because the $q\phi_B$ is theoretically inverse proportional to the work function of the Ag electrode. As previous reports, it is exemplified that the work function of AgNP is higher than that of bulk Ag metal from both theoretical and experimental results.^{43,44} Therefore, the increment of work function strongly indicates that AgNPs exist on the Ag electrode surface contacting to the *p*-Si, in which the existence of AgNPs is also implied from surface roughness. Furthermore, free electrons possessed by a metal nanoparticle should be depleted easier than bulk metal. The supply of electron to the outer AgNPs on the

Ag electrode surface cannot keep up with the demand for conduction if electron mobility is limited in the sub-nanometer to micrometer scale in the printed Ag electrodes. Thus, the increment of barrier height can be expressed qualitatively by the depletion of the electrons at the Ag/*p*-Si interface due to the existence of AgNPs on the Ag electrode surface.

Considering Schottky barrier diode, the charge transfer occurs between metal and semiconductor, and then a depletion contact is formed at the interface of metal/semiconductor contact. For contacts on semiconductors, the depletion-layer width, W is given by

$$W = \sqrt{\frac{2\varepsilon\phi_{bi}}{qN_d}} \quad (6)$$

Table 2. Surface-averaged roughness, CPD and estimated work function of the printed and vacuum-deposited Ag electrodes in AFM/KPFM.

Ag electrode	Sintering time (min)	Surface roughness (nm) ^a	CPD (V)	Work function (eV) ^b
Printed	5	29.2	0.61	4.49
	7.5	26.8	0.31	4.79
	10	14.1	0.39	4.71
	15	5.8	0.23	4.87
	30	3.8	0.17	4.93
Vacuum-deposited	—	2.8	0.42	4.68

^a Surface roughness is defined as the equation of $\frac{1}{n} \sum |h_{ave} - h_k|$. Here, n is the number of data points, h_{ave} is the averaged-height value, and h_k is the height value of at every data point, respectively. ^b Work function of the electrodes were estimated by referring of the typical work function value of Au (5.10 eV).

where ϵ , ϕ_{bi} , q , and N_d are permittivity of semiconductor, built-in potential, electronic charge and doping density of semiconductor, respectively.^{1,2} Using built-in potential, Schottky barrier height, ϕ_B is given by

$$\phi_B = V_0 + \phi_{bi} \quad (7)$$

where V_0 is too low (< 0.05 eV) enough to be ignored when the doping density of the semiconductor is low ($N_d < 10^{16} \text{ cm}^{-3}$). Thus, in our case ($N_d \approx 10^{15} \text{ cm}^{-3}$), Schottky barrier height, ϕ_B can be approximated to be $\phi_B \approx \phi_{bi}$ from equation (7). From equation (6) and (7), the depletion-layer width, W can be obtained as

$$W^2 \approx \frac{2\epsilon\phi_B}{qN_d} \quad (8)$$

Consequently, the ϕ_B is approximately proportional to the square of W as shown in the following equation.

$$\phi_B \propto W^2 \quad (9)$$

This relationship can explain the increment of barrier height in the printed SBDs. In the Ag/ p -Si interface, the charge transfer occurs from the AgNPs attached on the Ag electrode surface to p -Si developing partial positive charges at the Ag electrode surface. The formed depletion layer spreads and becomes thicker in the depth, because electron mobility is limited in the printed Ag electrodes due to cracks and boundary defects in the electrodes. Increased thickness of depletion layer (W) can then increase the apparent barrier height (ϕ_B) as predicted based on

the equation (9), though the existence of AgNPs at the interface leads to the increase in the work function (up to 0.25 eV as compared to that of an vacuum-deposited Ag electrode).

Conclusions

In conclusion, we provided a first demonstration of the Si-based printed SBDs, where the Ag electrodes were formed by the printing of AgInk on the p -Si and sintering, and in-depth description of the electronic-energy state at the Ag/ p -Si interface in the printed SBDs. For fabrication of the printed SBDs, monodispersed AgNPs stabilized with tetradecanoic acid were synthesized and used as the precursor for preparation of AgInk. Using the AgInk, the Ag electrodes were successfully fabricated by printing and sintering on the p -Si. The resulting SBDs showed typical I-V characteristics and relatively high rectification ratio compared with vacuum-deposited Ag electrode. From the numerical analyses of I-V data, the Schottky parameters were successfully estimated, in which the parameters showed sintering time dependent behavior. Especially, the Schottky barrier height is 0.14 eV higher in the sintering time of 30min compared with a vacuum-deposited SBD. To clarify the unprecedented electrical characteristics of the printed SBDs, observations of SEM and AFM/KPFM were conducted. From cross-sectional SEM observations, it was found that micrometer size of pores emerge at the Ag/ p -Si interface due to the removal of the solvent and other organics in the AgInk. These morphological results strongly suggest that the increment of n and r_s of the Schottky parameters are responsible for the interface deviates from the ideal contact by the emergence of pores, in which the fluency of electrons and holes should be hindered. On the other hand, from the EDX elemental mapping of the cross-section, there was no evidence of an oxide layer and/or an alloyed layer in the Ag/ p -Si interface. Further investigations by AFM/KPFM observations in the

Ag/*p*-Si interface indicated that the surface potential of the printed Ag electrodes decreases with increasing sintering time. Interestingly, the estimated work function of the printed Ag electrode were higher than the theoretical work function of metal Ag, indicating that AgNPs exist on the electrode surface because the work function of AgNP is higher than the work function of metal Ag. Thus, in the Ag/*p*-Si interface, the charge transfer occurs from the AgNPs to *p*-Si, resulting in the formation and development of the depletion layer. Development of depletion layer in the depth increases the apparent barrier height because the barrier height is approximately proportional to the square of thickness of the depletion layer. This is an expected step in the increment of the barrier height, and thus the origin of the unprecedented high rectification ratio in the printed SBDs. These results imply that engineering of barrier height can be possible by the control of nanoparticle size and the number of nanoparticles emerged on the surface contacted to the semiconductor, which is not only beneficial way for the engineering of metal/semiconductor, but also for the printed electronics to achieve next-generation devices.

Methods

Materials

Sodium hydroxide (99%, Wako Pure Chemical Industries Ltd.), *n*-octanoic acid (99%, Tokyo Chemical Industry Co., Ltd.), silver nitride (> 99%, Tokyo Chemical Industry Co., Ltd.), tetradecanoic acid (> 99%, Wako Pure Chemical Industries Ltd.), octadecylamine (99%, Wako Pure Chemical Industries Ltd.), 1-octadecene (> 99%, Tokyo Chemical Industry Co. Ltd.), *p*-tert butyltoluene (> 99.8%, Wako Pure Chemical Industries Ltd.), and 2-phenylethan-1-ol (> 99.8%, Wako Pure Chemical Industries Ltd.), ETHOCEL® (STD100, Nisshin Kasei Co., Ltd.) were purchased and employed in the preparation without further purification. Silicon wafers (*p*-Si, B-doped, 3–7 Ω·cm) were purchased from ELECTRONICS AND MATERIALS CORPORATION Ltd. Prior to experiments, *p*-Si wafers were cut and washed with the mixed solvent composed of ethanol and acetone (1:1) three times. Next, placed 6 mL of NH₄OH (30 wt%) and 30 mL of deionized water in a glass beaker and then heated to 80 °C. To this solution, 6 mL of H₂O₂ (30 wt%) was added. Then, the *p*-Si was immersed in the solution and kept for 30 min at 80 °C. Finally, the *p*-Si was rinsed with deionized water and then dried using an air blower.

Synthesis of silver(I)–octanoate complex

Silver(I)–octanoate complex was prepared by the similar synthetic procedure of silver(I)–alkanoates complex. In a typical synthesis of silver(I)–octanoate complex, 2.00 g of

sodium hydroxide (50.0 mmol) in 50 mL of ethanol was added to 7.21 g of *n*-octanoic acid (50.0 mmol) in 50 mL of ethanol. The resulting solution was stirred at 80 °C. After stirring for one hour, 8.58 g of silver nitride (50.0 mmol) in 25 mL of deionized water was added to the solution, resulting in immediate precipitation of a white solid. Stirring overnight at ambient temperature, the precipitate was collected by vacuum filtration, washed several times with hot deionized water in a Buchner funnel and dried in vacuo for overnight, resulting in silver(I)–octanoate complex in an off-white solid form, 11.50 g (yield: 91.7 %).

Synthesis of silver nanoparticles (AgNPs)

In the typical synthetic procedure for AgNPS with an average diameter of 8 nm, 9.14 g of tetradecanoic acid (40.0 mmol), 10.78 g of octadecylamine (40.0 mmol), and 10.20 g of 1-octadecene were placed in a flask and heated to 120 °C with vigorous stirring. In the resulting homogeneous solution, 10.04 g of the silver(I)–octanoate complex (40.0 mmol) was added and raised the temperature to 180 °C. The reaction was proceeded with vigorous stirring at 180 °C for 2 h. After reaction, the solution was cooled to ambient temperature, and washed three times with 2-propanol. After drying under ambient atmosphere for overnight, AgNPs as dark blue solid were obtained (5.12 g).

Preparation of silver nanoink (AgInk)

For preparing AgInk, 0.556 g of the AgNPs were added in 1.497 g of the solution composed of *p*-tert butyltoluene (1.422 g), 2-phenylethan-1-ol (0.075 g), and ETHOCEL® (0.150 g). To homogenize carefully, mixing operation was performed with a planetary mixing apparatus (Kurabo, Mazerustar, KK-250S). The mixing was performed for three times with revolution of 1600 rpm and rotation of 1600 rpm for 10 min. After mixing procedure, the AgNPs were dispersed uniformly, achieving AgInk with the desired silver content.

Fabrication of Schottky barrier diode by squeegee method

Fabrication of Schottky barrier diode was performed in two steps. Before all steps, for removing SiO₂ layer, the *p*-Si was immersed in aqueous hydrogen fluoride solution (2 wt%) for 1 min, rinsed with deionized water, and then dried with an air blower. First, on a side of the *p*-Si, deposition of aluminum (Al) as an ohmic electrode was performed using an evaporation system (ULVAC, VPC-260F, pressure 2×10^{-3} Pa, current 28 A, evaporation time 3 min). After deposition of Al, for making ohmic contacts possible in the Al/*p*-Si interface, the *p*-Si after deposition was placed in an oven and annealed at 500 °C for 7 min. Next, on

the other side, AgInk was patterned by squeegee method which is one of printing methods. In this method, on the *p*-Si, a pit (size: $0.15 \times 0.15 \text{ cm}^2$) was constructed from 0.100 mm thick masking tape (Nitto Denko Corporation, N-300). A small amount of AgInk was placed onto the pit and then excess amount of AgInk was removed with a metal blade. After drying on a hot plate at 60 °C for 5 min, the masking tape was peeled away, achieving a smooth thin layer was formed. The patterned *p*-Si was then placed in an oven at 300 °C and sintered for the desired time (5, 7.5, 10, 15, and 30 min).

Measurements

The prepared AgNPs were characterized by TEM (JEOL, JEM-2010, accelerating voltage 100 kV). The metal content of AgNPs and AgInk were estimated by thermogravimetric analysis using a thermal analysis system (Rigaku, Thermo plus Evo) from room temperature to 500 °C with a heating rate of $20 \text{ }^\circ\text{C} \cdot \text{min}^{-1}$ under an air flow of $300 \text{ mL} \cdot \text{min}^{-1}$. Sheet resistance of the sintered silver films were measured using a resistivity meter (Mitsubishi analytech, Loresta-GP). Measurements of I-V characteristics of the Schottky barrier diodes were performed using a Current/Voltage monitor (ADCMT, 6241A) and a manual prober (ESS Tech, SP-0-3Ls). Morphological observations and EDX analyses of the silver electrodes were performed by FE-SEM with an energy dispersive X-ray spectrometer (JEOL, JSM-7800F, voltage 5 kV, WD 10 mm). Images of atomic force microscopy (AFM) and Kelvin probe force microscopy (KPFM) were taken by scanning probe microscopy (Shimadzu, SPM-9700HT). AFM and KPFM measurements were performed in the force modulation mode using a platinum silicide coated cantilever (NanoWorld AG, PtSi-FM, tip curvature <25 nm, spring constant $2.8 \text{ N} \cdot \text{m}^{-1}$, resonant frequency 75 kHz) under ambient atmosphere.

Acknowledgements

This work was performed using the facility at Osaka Research Institute of Industrial Science and Technology (ORIST). This work was partially supported by the JSPS KAKENHI (Grant Number 18K14131). In addition, special thanks for several experiments and insightful comments from Dr. Masaya Chigane.

Author Contributions

M.S. and T.T. designed the research plan and discussed the results. M.S. performed all experiments and wrote the paper. The manuscript was reviewed and edited by M.S. and T.T. All

authors approved the final version.

Additional Information

Competing Interests

The authors declare no competing interests.

References

- Schroder, D. K. *Semiconductor Material and Device Characterization* 3rd ed. (Wiley, 2006).
- Sze, S. M. & Ng, K. K. *Physics of Semiconductor Devices* 3rd ed. (Wiley, 2007).
- Tung, R. T. The physics and chemistry of the Schottky barrier height. *Appl. Phys. Rev.* **1**, 011304 (2014).
- Li, S. S. *Semiconductor Physical Electronics* 2nd ed. (Springer, 2006).
- Kang, K. *et al.* Layer-by-Layer assembly of two-dimensional materials into wafer-scale heterostructures. *Nature* **550**, 229–233 (2017).
- Liu, Y. *et al.* Approaching the Schottky-Mott limit in van der Waals metal-semiconductor junctions. *Nature* **557**, 696–700 (2018).
- Lewis, J. A. Direct ink writing of 3D functional materials. *Adv. Funct. Mater.* **16**, 2193–2204 (2006).
- Perelaer, J. *et al.* Printed electronics: the challenges involved in printing devices, interconnects, and contacts based on inorganic materials. *J. Mater. Chem.* **20**, 8446–8453 (2010).
- Suganuma, K. *Introduction to Printed Electronics* (Springer, 2014).
- Kamyshny, A. & Magdassi, S. Conductive nanomaterials for printed electronics. *Small* **10**, 3515–3535 (2014).
- Wu, W. Inorganic nanomaterials for printed electronics: a review. *Nanoscale* **9**, 7342–7372 (2017).
- Farahani, R. D., Dubé, M. & Theriault, D. Three-dimensional printing of multifunctional nanocomposites-manufacturing techniques and applications. *Adv. Mater.* **28**, 5794–5821 (2016).
- Matsui, H., Takeda, Y. & Tokito, S. Flexible and printed organic transistors: from materials to integrated circuits. *Org. Electron.* **75**, 105432 (2019).
- Chow, P. C. Y. & Someya, T. Organic photodetectors for next-Generation wearable electronics. *Adv. Mater.* **32**, 1902045 (2020).
- Kang, H., Kitsomboonloha, R., Jang, J. & Subramanian, V. High-performance printed transistors realized using femtoliter gravure-printed sub-10 μm metallic nanoparticle patterns and highly uniform polymer

- dielectric and semiconductor layers. *Adv. Mater.* **24**, 3065–3069 (2012).
16. Grau, G. *et al.* Gravure-printed electronics: recent progress in tooling development, understanding of printing physics, and realization of printed devices. *Flex. Print. Electron.* **1**, 023002 (2016).
17. Ye, S., Rathmell, A. R., Chen, Z., Stewart, I. E. & Wiley, B. J. Metal nanowire networks: the next generation of transparent conductors. *Adv. Mater.* **26**, 6670–6687 (2014).
18. Bonaccorso, F., Bartolotta, A., Coleman, J. N. & Backes, C. 2D-crystal-based functional inks. *Adv. Mater.* **28**, 6136–6166 (2016).
19. Fukuda, K. & Someya, T. Recent progress in the development of printed thin-film transistors and circuits with high-resolution printing technology. *Adv. Mater.* **29**, 1602736 (2017).
20. Gu, W. *et al.* Fast near infrared sintering of silver nanoparticle ink and applications for flexible hybrid circuits. *RSC Adv.* **8**, 30215–30222 (2018).
21. Garlapati, S. K. *et al.* Printed electronics based on inorganic semiconductors: from processes and materials to devices. *Adv. Mater.* **30**, 1707600 (2018).
22. Kim, D., Jeong, S., Shin, H., Xia, Y. & Moon, J. Heterogeneous interfacial properties of ink-jet-printed silver nanoparticulate electrode and organic semiconductor. *Adv. Mater.* **20**, 3084–3089 (2008).
23. Wang, W., Chen, X. & Efrima, S. Silver nanoparticles capped by long-chain unsaturated carboxylates. *J. Phys. Chem. B* **103**, 7238–7246 (1999).
24. Binnemans, K., Van Deun, R., Thijs, B., Vanwelkenhuysen, I. & Geuens, I. Structure and mesomorphism of silver alkanoates. *Chem. Mater.* **16**, 2021–2027 (2004).
25. Wünscher, S., Abbel, R., Perelaerabd, J. & Schubert, U. S. Progress of alternative sintering approaches of inkjet-printed metal inks and their application for manufacturing of flexible electronic devices. *J. Mater. Chem. C* **2**, 10232–10261 (2014).
26. Michaelson, H. B. The work function of the elements and its periodicity. *J. Appl. Phys.* **48**, 4729–4733 (1977).
27. Smith, B. L. & Rhoderick, E. H. Schottky barriers on p-type silicon. *Solid State Electron.* **14**, 71–75 (1971).
28. Li, S. S. *Semiconductor Physical Electronics* 2nd ed. Ch. 10, p310, Table 10.3 (Springer, 2006).
29. Norde, H. A modified forward IV plot for Schottky diodes with high series resistance. *J. Appl. Phys.* **50**, 5052–5053 (1979).
30. Lien, C.-D., So, F. C. T. & Nicolet, M.-A. An improved forward I-V method for nonideal Schottky diodes with high series resistance. *IEEE Trans. Electron Devices* **ED-31**, 1502–1503 (1984).
31. Cibils, R. M. & Buitrago, R. H. Forward I-V plot for nonideal Schottky diodes with high series resistance. *J. Appl. Phys.* **58**, 1075–1077 (1985).
32. Sato, K. & Yasumura, Y. Study of forward IV plot for Schottky diodes with high series resistance. *J. Appl. Phys.* **58**, 3655–3677 (1985).
33. Lee, T. C., Fung, S., Beling, C. D. & Au, H. L. A systematic approach to the measurement of ideality factor, series resistance, and barrier height for Schottky diodes. *J. Appl. Phys.* **72**, 4739–4742 (1992).
34. Cheung, S. K. & Cheung, N. W. Extraction of Schottky diode parameters from forward current-voltage characteristics. *Appl. Phys. Lett.* **49**, 85–87 (1986).
35. Andrews, J. M. & Lepselter, M. P. Reverse current-voltage characteristics of metal-silicide Schottky diodes. *Solid State Electron.* **13**, 1011–1023 (1970).
36. Ide, E., Angata, S., Hirose, A. & Kobayashi, K. F. Metal-metal bonding process using Ag metallo-organic nanoparticles. *Acta Mater.* **53**, 2385–2393 (2005).
37. Peng, P. *et al.* Joining of silver nanomaterials at low temperatures: processes, properties, and applications. *ACS Appl. Mater. Interfaces* **7**, 12597–12618 (2015).
38. Jia, J. F., Inoue, K., Hasegawa, Y., Yang, W. S. & Sakurai, T. Local work function for Cu(111)–Au surface studied by scanning tunneling microscopy. *J. Vac. Sci. Technol. B* **15**, 1861–1864 (1997).
39. Nonnenmacher, M., O’Boyle, M. P. & Wickramasinghe, H. K. Kelvin probe force microscopy. *Appl. Phys. Lett.* **58**, 2921–2923 (1991).
40. Vatel, O. & Tanimoto, M. Kelvin probe force microscopy for potential distribution measurement of semiconductor devices. *J. Appl. Phys.* **77**, 2358–2362 (1995).
41. Zerweck, U., Loppacher, C., Otto, T., Grafström, S. & Eng, L. M. Accuracy and resolution limits of Kelvin probe force microscopy. *Phys. Rev. B* **71**, 125424 (2005).
42. Wang, P., *et al.* Silver nanoparticles with tunable work functions. *Appl. Phys. Lett.* **107**, 151601 (2015).
43. Schnippering, M., Carrara, M., Foelske, A., Kötz, R. & Fermín, D. J. Electronic properties of Ag nanoparticle arrays. A Kelvin probe and high resolution XPS study. *Phys. Chem. Chem. Phys.* **9**, 725–730 (2007).
44. Dadlani, A. L., Schindler, P., Logar, M., Walch, S. P. & Prinz, F. B. Energy States of Ligand Capped Ag Nanoparticles Relating Surface Plasmon Resonance to Work Function. *J. Phys. Chem. C* **118**, 24827–24832 (2014).